

On the Interplay between CH \cdots O and OH \cdots O Interactions in Determining Crystal Packing and Molecular Conformation: An Experimental and Theoretical Charge Density Study of the Fungal Secondary Metabolite Austdiol (C₁₂H₁₂O₅)

Leonardo Lo Presti,^{*,†} Raffaella Soave,[‡] and Riccardo Destro[†]

Dipartimento di Chimica Fisica ed Elettrochimica, Università di Milano, Via Golgi 19, 20133 Milano, Italy, and CNR-ISTM, Istituto di Scienze e Tecnologie Molecolari, Via Golgi 19, 20133 Milano, Italy

Received: November 24, 2005; In Final Form: February 3, 2006

The total experimental electron density $\rho(\mathbf{r})$, its Laplacian $\nabla^2\rho(\mathbf{r})$, the molecular dipole moment, the electrostatic potential $\varphi(\mathbf{r})$, and the intermolecular interaction energies have been obtained from an extensive set of single-crystal X-ray diffracted intensities, collected at $T = 70(1)$ K, for the fungal metabolite austdiol (**1**). The experimental results have been compared with theoretical densities from DFT calculations on the isolated molecule and with fully periodic calculations. The crystal structure of (**1**) consists of zigzag ribbons extended along one cell axis and formed by molecules connected by both OH \cdots O and CH \cdots O interactions, while in a perpendicular direction, adjacent molecules are linked by short CH \cdots O intermolecular contacts. An extensive, quantitative study of all the intra- and intermolecular H \cdots O interactions, based not only on geometrical criteria, but also on the topological analysis of $\rho(\mathbf{r})$, as well as on the evaluation of the pertinent energetics, allowed us (i) to assess the mutual role of OH \cdots O and CH \cdots O interactions in determining molecular conformation and crystal packing; (ii) to identify those CH \cdots O contacts which are true hydrogen bonds (HBs); (iii) to determine the relative hydrogen bond strengths. An experimental, quantitative evidence is given that CH \cdots O HBs are very similar to the conventional OH \cdots O HBs, albeit generally weaker. The comparison between experimental and theoretical electric dipole moments indicates that a noticeable charge rearrangement occurs upon crystallization and shows the effects of the mutual cooperation of HBs in the crystal. The total intermolecular interaction energies and the electrostatic energy contribution obtained through different theoretical methods are reported and compared with the experimental results. It is found that the new approach proposed by Spackman, based on the use of the promolecular charge density to approximate the penetration contribution to intermolecular electrostatic energies, predicts the correct relative electrostatic interaction energies in most of the cases.

1. Introduction

A detailed knowledge of the forces that determine the structural motifs of crystalline materials is a major aim in solid-state chemistry and forms the basis of crystal engineering. Hydrogen bonds (HBs), in view of their energy and directionality, play a crucial role in supramolecular organization and are among the most important factors that determine the packing of molecular crystals.^{1,2} The literature concerning this topic is very rich and spans through the fields of crystal engineering,^{3,4} crystal structure prediction,^{5–7} supramolecular chemistry,^{8–10} and intermolecular recognition.^{11–14} In particular, the understanding of the mutual interplay between HBs of different strength, and between intra- and intermolecular interactions, is crucial in the formulation of general rules for the packing of hydrogen-bonded crystals.^{15–17} Among others, two simple rules have been proposed in recent years:¹⁸ (1) “All hydrogen bond acceptors available in a molecule will be engaged in hydrogen bonding as far as there are available donors”, and (2) “The hydrogen bond acceptors will be saturated in order of decreasing strength of the hydrogen bond formed”. The last statement implicitly points out that, not only the stronger OH \cdots O HBs, but also the weaker, unconventional CH \cdots Y interactions, such

as CH \cdots O, are to be considered in order to correctly describe the hydrogen bond pattern of a crystal.

Nowadays, the reliability of CH \cdots O bonding is well assessed;^{19,20} thanks to the surge of interest toward statistical database surveys and to the increasing application of sets of criteria such as those of Koch and Popelier,^{21–25} the fundamental properties of these interactions have been elucidated, and it has been shown that they may behave very much like a conventional OH \cdots O HB in most respects.^{22,25} However, some features deserve further investigation. In particular, the following questions are worthy of note: (1) Which is the mutual role of OH \cdots O and CH \cdots O interactions in governing the packing of hydrogen-bonded crystals? (2) May CH \cdots O be competitive with stronger HBs in determining the molecular conformation and crystal packing? (3) Do CH \cdots O and OH \cdots O HBs fit the same topological and energetic pattern?

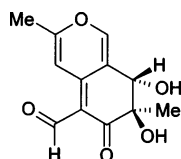
Conclusions upon hydrogen bonding are often drawn via purely geometrical criteria, but it is now well established that the quantum theory of atoms in molecules (QTAIM)²⁶ adds further information to that obtained from the conventional structural analysis, and it is to be recommended if a full characterization of such bonds is desired. A detailed topological analysis of the electron density distribution $\rho(\mathbf{r})$ in a hydrogen-bonded crystal may indeed quantitatively characterize the interplay between competing interactions. Furthermore, it provides relationships between charge density and geometrical

* To whom correspondence should be addressed. E-mail: leonardo.lopresti@unimi.it.

[†] Dipartimento di Chimica Fisica ed Elettrochimica.

[‡] Istituto di Scienze e Tecnologie Molecolari.

SCHEME 1



parameters that are essential in the quantitative determination of the strength of the bond.²⁷

To this end, it is clearly of interest to correlate the local density values at the HB bcp, obtained from the topological analysis of the $\rho(\mathbf{r})$, to the total energy of the bond, as in the approaches proposed by Abramov²⁸ and Espinosa et al.²⁵ As already outlined by Coppens and co-workers,²⁹ it must be noted that the theoretical and experimental values of the total intermolecular interaction energy (E_{int}) should not be quantitatively associated with the HB energy, as the intermolecular HBs are not the only and not necessarily the main contributions to E_{int} .

In this paper, our central aim is to use the topological and energetic properties obtained from an X-ray diffraction experiment, in addition to the usual geometrical tools, to answer the three questions above. A medium-size, heavily functionalized molecule such as austdiol (**1**) (see Scheme 1), with an aldehyde, a *trans*-vicinal diol, a keto group, a pyranic oxygen atom, and both O–H and C–H hydrogen bond donors, appears as a fitting case.

The fungal metabolite (**1**) is the main toxic component of a mixture of substances produced in mouldy maize meal by cultures of *Aspergillus ustus*.^{30,31} So far, (**1**) has been studied by means of chemical and spectroscopic^{32–35} techniques and by a room-temperature (RT) single-crystal X-ray diffraction experiment.³⁶ In the latter investigation, the absolute configuration of the two stereocenters was based on the known configuration from an earlier X-ray study of the 5-bromo derivative.³⁷

In this work, the total X-ray charge distribution $\rho(\mathbf{r})$ of (**1**) at $T = 70$ K is analyzed according to the Bader's QTAIM²⁶ and compared with DFT results on the isolated molecule. In the first part, the results of a combined experimental and theoretical study of all the intra- and intermolecular XH...O interactions ($X = \text{C}, \text{O}$) are presented, following these steps: (i) geometrical investigation of the molecular conformation and crystal packing; (ii) topological characterization of XH...O contacts and their classification on the basis of the Koch and Popelier criteria;²¹ (iii) estimate of the hydrogen bond energetics from the topological properties.

In the second part of the paper, the results of the evaluation of the electrostatic properties of (**1**), including the molecular dipole moments, the electrostatic potential $\varphi(\mathbf{r})$, and the energies of the intermolecular interactions are reported as follows: (i) comparison between molecular dipole moments as derived from the X-ray $\rho(\mathbf{r})$ in the crystal and the DFT distribution on the isolated molecule; (ii) investigation of the experimental $\varphi(\mathbf{r})$; (iii) comparison between theoretical (both on the isolated molecule and on the crystal) and experimental estimates of E_{int} and focus on the electrostatic contribution (E_{es}) to the total energy.

2. Methods

2.1. X-ray Diffraction. The pale-orange crystal selected for the data collection was slowly crystallized from a H₂O–MeOH 95:5 solution; its quality was checked by diffraction photographs on a modified³⁸ four-circle Syntex P1 diffractometer equipped with a Samson cryostat.³⁹

TABLE 1: Crystallographic Details

sample information	
empirical formula	C ₁₂ H ₁₂ O ₅
crystal size, mm ³	0.50 × 0.30 × 0.23
formula wt, g mol ^{−1}	236.22
crystal system	orthorhombic
space group	P2 ₁ 2 ₁ 2 (no. 18)
Z	4
T, K	70(1)
a, Å	8.4175(9)
b, Å	19.8668(20)
c, Å	6.2843(9)
V, Å ³	1050.9(2)
ρ _{calcd} , g cm ^{−3}	1.493
F(000)	496
μ, mm ^{−1}	0.11
data collection	
λ, Å	0.71073
(sin θ/λ) _{max} , Å ^{−1}	1.00
scan type	ω − 2θ
scan rate, deg min ^{−1}	3.0
scan range (2θ), deg ^a	2.4
no. of collected reflns	20599
no. of unique reflns	4898
no. of observed reflns (I > 0, N _{obs})	4696
refinement results	
GOF	1.2194
R(F), R(F ²) ^b	0.0269, 0.0229
R _w (F ²) ^b	0.0482
R(F), R(F ²) ^c	0.0119, 0.0155
R _w (F ²) ^c	0.0297
no. of variables (N _v)	687
N _{obs} /N _v	6.8

^a The angular separation between the $K_{\alpha 1}$ and the $K_{\alpha 2}$ components of the incident radiation is not included. ^b R values for all data ^c R values for 1402 data with $\sin \theta / \lambda \leq 0.65$ Å^{−1}

Unit cell dimensions at 70 K (Table 1) were obtained from 150 measures of the setting angles of 15 reflections with 2θ in the range 26–32°. A total of 20 599 intensities have been collected at $T = 70(1)$ K⁴⁰ up to a 2θ value of 90° for graphite-monochromated Mo K α radiation ($\sin \theta / \lambda = 1.00$ Å^{−1}). Weighted averaging of multiple data yielded 4898 independent reflections, of which 4696 were observed ($I > 0$). Full crystallographic and data-collection details are given in Table 1. The electron density was obtained from the diffraction data by a multipolar expansion of atom-centered functions according to the rigid pseudoatom formalism of Stewart.⁴¹ The final model employed a multipolar expansion up to the hexadecapole level ($l = 4$) on C and O atoms and to the quadrupole level ($l = 2$) on H atoms. All refinements were carried out with the VALRAY⁴² program, and the final results are reported in Table 1.

For all the 12 H atoms, anisotropic displacement parameters (ADP's) were evaluated with the method proposed by Roversi and Destro⁴³ and included in the final model. The Hirshfeld rigid bond test⁴⁴ and the rigid-body TLS analysis⁴⁵ were performed to check the quality of the refined ADP's. Because the differences between the mean-square displacement amplitudes (MSDA's) along bond directions have a mean value of 0.00035(19) Å² for the 18 covalent bonds not involving H atoms, the rigid bond postulate appears well satisfied. The results of the TLS analysis confirm that the molecule, as expected, can be considered as a rigid body after exclusion of the exocyclic groups.

2.2. Theoretical Calculations. A full conformational analysis of the system under study has been carried out with the MACROMODEL⁴⁶ 5.0 program (MM2⁴⁷ force field) to inves-

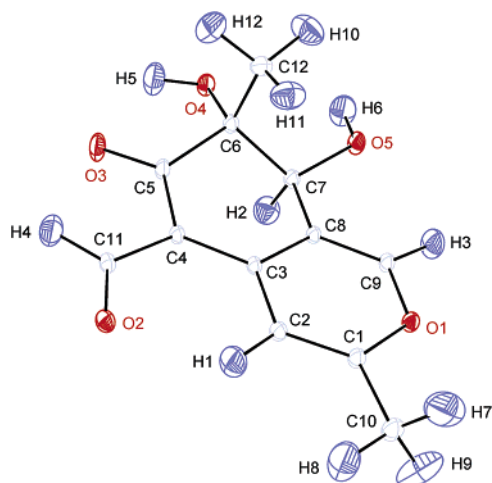


Figure 1. ORTEP plot of austdiol at 70 K, with the atom numbering scheme. Ellipsoids at 50% probability level.

tigate whether the solid state conformation of (**1**) differs from the gas-phase conformation. A complete discussion of the molecular mechanics (MM) calculations can be found in the Supporting Information.

Both the 70 K experimental geometry and the lowest-energy MM2 conformer have been used as starting points for the DFT optimization of the isolated molecule with the GAUSSIAN98⁴⁸ (G98) program. Single-point calculations have then been performed on the austdiol molecule and on five isolated dimers at the experimental geometry with both the G98⁴⁸ and the ADF2004.01^{49,50} programs. In the G98 calculations, the standard 6-31G(p,d) basis set and the B3LYP^{51,52} hybrid-type functional were used, while in the ADF calculations, we have adopted the standard triple- ζ exponential (TZP) basis set and the BLYP^{52,53} functional, within the generalized gradient approximation (GGA). The dimer interaction energies have been calculated by taking into account the correction for the basis set superposition error (BSSE) by the counterpoise method.⁵⁴

Fully periodic DFT calculations at the 70 K experimental geometry were carried out with the CRYSTAL03 program,⁵⁵ using the same exchange and correlation functionals and the same basis set as in the G98 calculations. A set of 4898 static structure factors (same hkl indices as in the X-ray experiment) in the range $0 < \sin \vartheta/\lambda < 1.0 \text{ \AA}^{-1}$ were obtained through Fourier transform of the theoretical, periodic $\rho(\mathbf{r})$. Only the charge density parameters (up to the hexadecapole level on C and O atoms and to the quadrupole level on H atoms, in analogy with the analysis of the experimental structure factors) were varied in the refinement of the theoretical F_c , using the code VALRAY.⁴² In the following and in the tables, the notations MG-B3LYP and MA-BLYP are used to distinguish molecular calculations (with GAUSSIAN and ADF, respectively) from those on the periodic crystal, which are marked as P-B3LYP.

3. Results and Discussion

3.1. Molecular Conformation and Crystal Packing. An ORTEP⁵⁶ plot of the austdiol molecule is shown in Figure 1. On going from RT to 70 K, no conformational change is observed. The six-membered ring of the cyclohexenone system has a distorted half-chair conformation, with puckering parameters⁵⁷ $Q = 0.4504(5) \text{ \AA}$, $\vartheta = 124.91(6)^\circ$, and $\phi = 278.44(8)^\circ$ for the atom sequence C8–C7–C6–C5–C4–C3. The pyran ring is almost perfectly planar, with deviations of the ring atoms from the mean ring plane ranging between $-0.0193(4) \text{ \AA}$ (atom C8) and $+0.0205(6) \text{ \AA}$ (atoms O1 and C3). The fused-ring

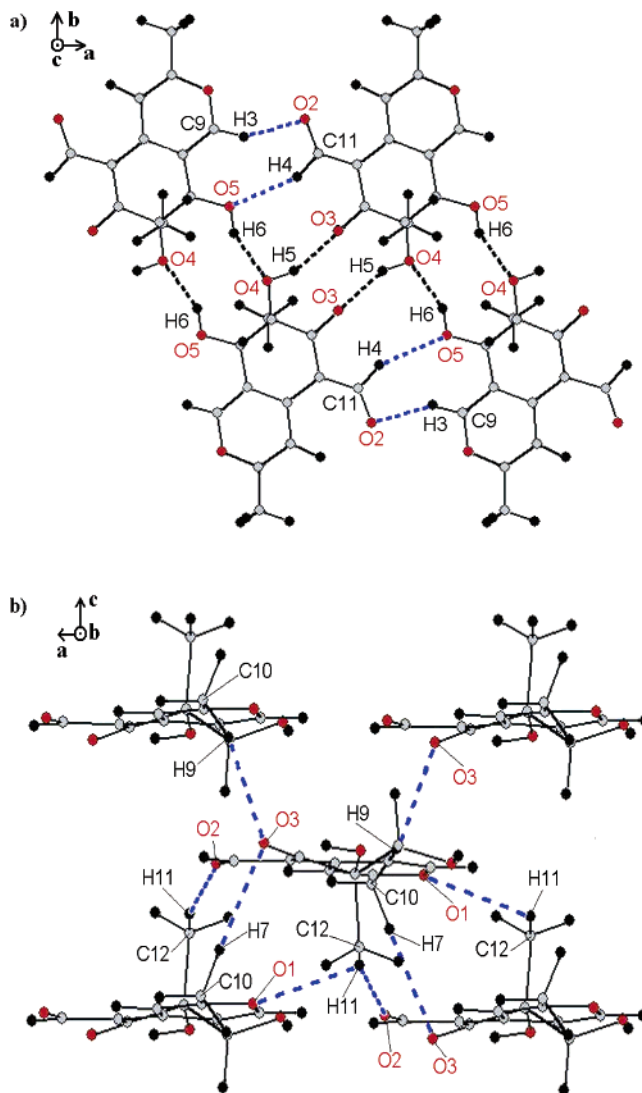


Figure 2. Packing diagram of (**1**) at 70 K, viewed down (a) the c axis, (b) the b axis. Intermolecular interactions are represented as black (OH \cdots O) and blue (CH \cdots O) dashed bonds.

system of the molecule lies nearly in the (a, b) plane, the angle between the crystallographic [001] direction and the normal to the least-squares plane defined by all the endocyclic atoms being $4.06(1)^\circ$.

As noted in the RT structure,³⁶ the exocyclic C1–C10 methyl bond is markedly shorter than the C6–C12 methyl bond ($1.4849(5) \text{ \AA}$ vs $1.5343(7) \text{ \AA}$ at 70 K). The difference is maintained also after the MG-B3LYP optimization (1.4923 \AA vs 1.5386 \AA) and indicates a hyperconjugative interaction^{58,59} of the C10 methyl group with the unsaturated system of (**1**). This has been confirmed by the topological analysis of the experimental $\rho(\mathbf{r})$.⁶⁰

The X-ray 70 K geometry has been employed as the starting point for an MG-B3LYP optimization of the isolated molecule: at convergence, the crystal conformation of the molecule is retained, with the C12 methyl group axial and the O5 hydroxy group equatorial.

The MM2 calculation indicates that the C12 methyl is equatorial in the minimum geometry (equatorial conformer). The axial conformer, whose energy is just $+0.44 \text{ kJ}\cdot\text{mol}^{-1}$ above the minimum, is almost exactly superimposable to the molecule as found in the crystal. By using the equatorial conformer geometry as a starting point for an MG-B3LYP optimization, the equatorial conformation of the C12 methyl is retained, but

TABLE 2: Experimental Contact Geometry and Topological Parameters of the XH...O (X = C, O) Interactions (First Row)^a

dimer	contact	HO, Å	XH, Å	XO, Å	XHO, deg	$\rho(\mathbf{r})_{\text{bcp}}^b$	$\nabla^2[\rho(\mathbf{r})_{\text{bcp}}]^b$	λ_1	λ_2	λ_3	ϵ^c
intramolecular interactions											
	C2–H1...O2	2.145(15) 2.137	1.092(15) 1.081	2.8743(5) 2.8730	121.8(10) 123.0	0.14(2) 0.143	1.79(13) 1.633	−0.566 −0.597	−0.458 −0.546	2.814 2.776	0.24 0.09
	C11–H4...O3	2.360(13) 2.416	1.095(13) 1.105	2.7769(7) 2.8476	100.5(8) 101.3	no bcp found no bcp found					
	O4–H5...O3	2.051(17) 1.983	0.947(18) 0.977	2.6188(7) 2.6201	116.9(12) 120.7	no bcp found 0.191	2.293	−0.849	−0.661	3.804	0.29
	O5–H6...O4	2.589(16) 2.430	0.929(18) 0.969	2.9295(6) 2.8599	102.2(11) 106.5	no bcp found no bcp found					
	C9–H3...O5	2.460(14) 2.440	1.061(15) 1.081	2.7147(5) 2.7303	92.1(8) 93.6	no bcp found no bcp found					
intermolecular interactions											
A	C12–H11...O1 ^d	2.979(14)	1.066(14)	3.5890(6)	116.9(9)	0.026(3)	0.37(1)	−0.072	−0.047	0.490	0.53
	C12–H11...O2 ^e	2.443(14)	1.066(14)	3.4778(6)	163.4(11)	0.06(1)	0.83(7)	−0.246	−0.207	1.281	0.19
	C10–H7...O3 ^e	2.544(18)	1.097(18)	3.6209(11)	166.9(12)	0.07(1)	0.81(4)	−0.232	−0.185	1.230	0.25
B	C7–H2...O2 ^f	2.798(13)	1.107(14)	3.4565(6)	117.8(8)	No bcp found					
	C10–H9...O3 ^f	2.420(20)	1.080(20)	3.4012(11)	150.5(13)	0.05(2)	0.67(10)	−0.185	−0.139	0.995	0.33
C	C11–H4...O5 ^g	2.519(14)	1.095(13)	3.5371(5)	154.1(10)	0.06(2)	0.79(33)	−0.218	−0.199	1.209	0.10
	C9–H3...O2 ^h	2.174(15)	1.061(15)	3.1422(5)	150.7(11)	0.13(2)	1.56(18)	−0.569	−0.498	2.626	0.14
D	O4–H5...O3 ⁱ	2.114(17)	0.947(18)	3.0142(7)	158.4(14)	0.13(2)	1.22(23)	−0.636	−0.527	2.378	0.21
E	O5–H6...O4 ^j	2.023(17)	0.929(18)	2.8836(6)	153.2(14)	0.14(2)	1.65(10)	−0.702	−0.601	2.954	0.17

^a s.u. in parentheses. For the intramolecular contacts, the optimized MG-B3LYP (second row) values are also reported. ^b The units are e Å^{−3} for the charge density and e Å^{−5} for the Laplacian and the three curvatures. ^c Bond ellipticity defined as $\epsilon = \lambda_1/\lambda_2 - 1$. ^d At 1/2 + X, 1/2 − Y, −Z. ^e At −1/2 + X, 1/2 − Y, −Z. ^f At −1/2 + X, 1/2 − Y, 1 − Z. ^g At 1 + X, +Y, +Z. ^h At −1 + X, +Y, +Z. ⁱ At 1 − X, 1 − Y, +Z. ^j At −X, 1 − Y, +Z.

its energy is higher than that of the axial conformer by +40.79 kJ·mol^{−1}. Hence, the conformation with the C12 methyl axial appears as the most stable in both the crystal and the gas phase.

Two main packing patterns can be recognized in (1). In the (*a*, *b*) plane (Figure 2a), the packing is dominated by the OH...O interactions involving the two hydroxyl and the keto groups, while the aldehyde group is involved in two short CH...O contacts. In this plane, each molecule is related to two different molecules in a head-to-head fashion by the 2-fold symmetry axis and to a third one by a unitary translation along the *a* axis. The overall motif is that of zigzag ribbons extended along the *a* axis, a pattern which is common in vicinal diols.¹⁷ In the *c* direction (Figure 2b), the ribbons are piled up, forming layers related by the screw axis and linked by CH...O interactions. The C12 methyl group extends in the free space between the layers, making a bifurcated short CH...O contact with the aldehyde and pyrane oxygen atoms of two adjacent molecules. In the same direction, the C10 methyl group forms two CH...O contacts involving the O3 keto oxygen atom of the molecule in the layers above and below. The geometrical parameters of all the independent XH...O (X = C, O) short contacts are summarized in Table 2, with standard uncertainties (s.u.) on the experimental quantities reported in parentheses.

3.2. Short XH...O Contacts. 3.2.1. Geometrical Investigation. Around the cyclohexenone ring, five short intramolecular contacts are present, all of them with a contact distance shorter than the sum of the van der Waals radii [1.70, 1.52, and 1.20 Å, for C, O, and H, respectively].⁶¹ Comparing these values with those from the MG-B3LYP optimization of an isolated molecule (Table 2), we see that the optimized values for the two O–H...O intramolecular contacts are markedly shorter than the experimental estimates. Conversely, the H...O distance in the C11–H4...O3 contact is significantly larger in the isolated molecule, while the other two interactions are the same, within 2 s.u.'s, in both experimental and theoretical results. We defer to the next section the discussion on the possible classification of such contacts as true HBs because we believe that the

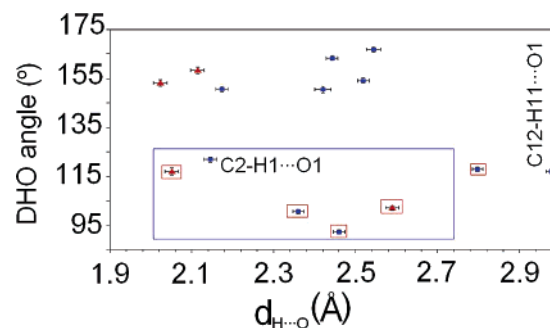


Figure 3. Values of the XHO angles (deg) vs H...O distances (Å) in (1). Intramolecular contacts are enclosed in a large blue box, while small red boxes enclose contacts that do not exhibit a bond path. Triangles: OH...O interactions; squares: CH...O interactions. Error bar size: 1 s.u.

topological descriptors of $\rho(\mathbf{r})$, and not only the geometrical parameters, are to be considered.

In Figure 3, the trend of the α_{XHO} angles versus the H...O distances ($d_{\text{H...O}}$) for the short intra- and intermolecular contacts, as obtained from the 70 K experiment, is reported. Following Steiner and Desiraju,²⁰ a long value of 3.0 Å as $d_{\text{H...O}}$ cutoff has been adopted, i.e., a value greater than sum of the van der Waals radii by 0.28 Å. In the figure, two main regions are evident, regardless of the $d_{\text{H...O}}$ distance and of the chemical nature of the HB donor. The upper one, above 150°, accounts for the almost flat, directional intermolecular interactions, with α_{XHO} values in the range 150–167°. The average angle for the CH...O contacts in this region is large (157(8)°) and very close to both the average OHO angle in the same zone (156(4)°) and to the value of 154.0(4)° reported in the literature⁶² for conventional OH...A (A = generic acceptor) HBs with hydroxy donors. The large and nearly constant CHO angle for these contacts indicates that the involved C–H donors are highly polarized and denotes the importance of the electrostatic energy contribution to such interactions. If the $d_{\text{H...O}}$ contact distance is considered, a marked similarity is observed between the two

OH...O HBs and the C9–H3...O2 interaction, the latter having a $d_{\text{H}\cdots\text{O}}$ value (2.174(15) Å) significantly shorter than the other CH...O contacts.

Conversely, the lower zone of the plot (below 125°) collects the five intramolecular contacts ($d_{\text{H}\cdots\text{O}}$ within 2.6 Å) plus the longer C7–H2...O2 and C12–H11...O1 intermolecular interactions ($d_{\text{H}\cdots\text{O}}$ higher than the sum of the van der Waals radii), which are all significantly bent.

In the next section, the full characterization of the nature of these contacts will be achieved with the aid of the topological analysis of $\rho(\mathbf{r})$.

3.2.2. Topological Characterization. Experimental electron distributions can be analyzed in terms of their topological features,⁶³ as theoretical charge distributions are, following the QTAIM theory.²⁶ Table 2 lists the geometrical and topological parameters of the *intramolecular* XH...O (X = C, O) short contacts, as obtained from the experimental data (first row) and from the MG-B3LYP optimization (second row). Experimental values for the *intermolecular* XH...O (X = C, O) interactions are also reported in the lower half of the table. The value of 3.0 Å has been selected as $d_{\text{H}\cdots\text{O}}$ cutoff to search for the existence of a bcp. In agreement with Gatti et al.,²³ from now on, we will name *bonded* only those contacts that are associated with an atomic interaction line (AIL) originating from a bcp between the H and O atoms, and we will term *nonbonded* those interactions which lack in the AIL, regardless of their $d_{\text{H}\cdots\text{O}}$ separation.

For all the bonded XH...O contacts in (1), the experimental electron density properties at bcp's are typical of conventional closed-shell interactions,²⁶ with the perpendicular curvatures λ_1 and λ_2 at bcp's small and nearly equal, and low values of bond ellipticity ϵ . Conversely, the parallel curvature, λ_3 , is roughly 1 order of magnitude greater than the other two. The $\rho_{\text{bcp}}(\mathbf{r})$ values are low and range from 0.026 e Å⁻³ (0.004 au) to 0.14 e Å⁻³ (0.021 au), well within the interval of 0.002–0.034 au reported by Koch and Popelier (hereinafter KP) for CH...O bonds in a set of four van der Waals complexes.²¹

Despite the steric accessibility of short contacts involving virtually stronger O–H donors, the only one intramolecularly bonded contact in the experimental $\rho(\mathbf{r})$ is a C–H...O, namely C2–H1...O2. It is favored over the other interactions by the formation of a planar six-membered conjugated ring, with rms deviation of the component atoms from the least-squares plane equal to 0.006 Å. Recently, it has been reported that the “involvement of a donor H in an intramolecular HB of this type makes it ca. three times less likely to be involved in the formation of intermolecular HBs than if the intramolecular HB was absent”.⁶⁴ This statement is exactly verified in (1) in the case of the C2–H1 donor, which indeed is not simultaneously involved in any competitive intermolecular HB. The $\rho_{\text{bcp}}(\mathbf{r})$ for H1...O2 is large and comparable with the corresponding values of the OH...O intermolecular HBs in this crystal (Table 2). Furthermore, as requested by the first KP criterion for hydrogen bonding,²¹ it has the correct topology of the gradient vector field: a rcp has been found near the centroid of the ring C11–C4–C3–C2–H1...O2, with $\rho_{\text{rcp}}(\mathbf{r})$ 0.74 Å far from the H1...O2 bcp, resulting in a topologically stable structure.²⁶ The sufficient criterion for the existence of an H bond is fulfilled, too, as a total mutual penetration of +0.078 Å has been found between H1 and O2. By comparing the experimental topological indicators for this bond with the optimized theoretical ones (Table 2), we see that they are the same within 1.2 s.u., indicating that the strength of this intramolecular interaction remains unchanged upon intermolecular HBs formation in the bulk and that it plays

an important role in the determination of the molecular conformation.

An opposite case of interplay between intra- and intermolecular interactions is given by the short O4–H5...O3 contact. All the MG-B3LYP calculations (on both the experimental and optimized geometry) find a bcp for this interaction (Table 2), which is not recovered in the experimental $\rho(\mathbf{r})$, neither with the present pseudoatom model nor with different multipolar expansions. The corresponding five-membered O4–H5...O3–C5–C6 ring deviates significantly from planarity (with distances of the ring atoms from the mean ring plane ranging between –0.13(2) and +0.1075(6) Å) and is not as stabilized as the previous six-membered motif. This explains why, in the crystal, where competing intermolecular interactions involving both H5 and O3 atoms occur, the intramolecular H5...O3 HB is absent. This is in agreement with the second rule proposed in ref 18.

Among the six CH...O intermolecularly bonded contacts, the C9–H3...O2 stands out for its similarity with the two OH...O bonded contacts, the former having a value of $\rho_{\text{bcp}}(\mathbf{r})$ equal to that of the O4–H5...O3 bond and about twice those of the other C–H...O bonds. The Laplacian values are all positive, from 0.37 e Å⁻⁵ (0.015 au) to 1.56 e Å⁻⁵ (0.065 au): the lowest value corresponds to the long C12–H11...O1 contact and is the only one out of the KP range (0.024–0.139 au), so invalidating one of the necessary criteria for the existence of an HB. This long contact (with $d_{\text{H}\cdots\text{O}} = 2.979(14)$ Å) is also characterized at its bcp by lower charge density, larger ϵ and smaller λ_3 than the other CH...O interactions. Moreover, the KP sufficient condition for the presence of a HB is not fulfilled by this interaction, as the O1 atom is more penetrated than the H11 atom by 0.050 Å.

Thus, at the end of this section, we feel confident in saying that (i) all the *bonded* contacts of Table 2, with the exception of the C12–H11...O1, which is better classified as a weak van der Waals interaction, are to be considered *true* HBs; (ii) CH...O HBs, while being generally weaker than the conventional OH...O, follow the same trend in terms of the topology of $\rho(\mathbf{r})$; (iii) one of them, namely C9–H3...O2, is also quantitatively comparable to OH...O HBs.

3.2.3. Hydrogen Bond Energetics from Topological Parameters. To gain a deeper insight into the fundamental nature of CH...O and OH...O HBs and to clarify which is their mutual role in the crystal, it is crucial to obtain reasonable estimates of their relative energies. To this end, for closed-shell interactions including HBs, the functional of Abramov²⁸ expresses the kinetic energy density $G(\mathbf{r})$ at the bcp's versus the experimental topological parameters:

$$G(\mathbf{r})_{\text{bcp}} = \frac{3}{10} \cdot (3\pi)^{2/3} \cdot \rho(\mathbf{r})_{\text{bcp}}^{5/3} + \frac{1}{6} \cdot \nabla^2 \rho(\mathbf{r})_{\text{bcp}} \quad (1)$$

The kinetic energy density $G(\mathbf{r})$ is in turn related to the potential energy density $V(\mathbf{r})$ through the local statement of the virial theorem:²⁶

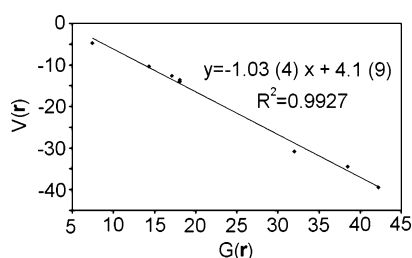
$$V(\mathbf{r})_{\text{bcp}} = \frac{\hbar^2}{4m} \nabla^2 \rho(\mathbf{r})_{\text{bcp}} - 2G(\mathbf{r})_{\text{bcp}} \quad (2)$$

The results obtained applying these relations to the experimental $\rho(\mathbf{r})$ of (1) for each of the bonded intermolecular interactions are listed in Table 3. The reported values of $V(\mathbf{r})_{\text{bcp}}$ are to be considered as estimates, as the multipole-derived charge density does not obey the local virial theorem.

TABLE 3: Estimates of the Kinetic Energy Density ($G(\mathbf{r})_{\text{bcp}}$), Local Potential Energy Density ($V(\mathbf{r})_{\text{bcp}}$), and Bond Energies ($-E_{\text{HB}}$) from the Experimental Topological Indicators of the Intermolecular $\text{XH}\cdots\text{O}$ HBs ($\text{X} = \text{C}, \text{O}$)^a

dimer	bond	$d_{\text{H}\cdots\text{O}}$	$G(\mathbf{r})^b$	$V(\mathbf{r})^c$	$-E_{\text{HB}}$ (eq 3) ^d	$-E_{\text{HB}}$ (eq 4) ^e
E	O5–H6 \cdots O4 ^f	2.023(17)	42.20	−39.44	19.7	12.3
D	O4–H5 \cdots O3 ^g	2.114(17)	31.96	−30.83	15.4	8.9
C	C9–H3 \cdots O2 ^h	2.174(15)	38.48	−34.49	17.3	9.5
B	C10–H9 \cdots O3 ⁱ	2.420(20)	14.30	−10.33	5.2	2.3
A	C12–H11 \cdots O2 ^j	2.443(14)	18.06	−13.55	6.8	3.0
C	C11–H4 \cdots O5 ^k	2.519(14)	17.10	−12.65	6.3	2.6
A	C10–H7 \cdots O3 ^l	2.544(18)	18.07	−13.99	7.0	2.8
A	C12–H11 \cdots O1 ^l	2.979(14)	7.45	−4.77	2.4	0.7

^a $d_{\text{H}\cdots\text{O}}$ in Å, $G(\mathbf{r})$, and $V(\mathbf{r})$ in units of kJ mol^{-1} per atomic unit volume, and E_{HB} in kJ mol^{-1} . ^b The kinetic energy density was evaluated according to ref 28. ^c The local potential energy density was evaluated by the application of the local statement of the virial theorem according to ref 25. ^d Estimated by eq 3: $E_{\text{HB}} = 0.5 \cdot V(\mathbf{r})_{\text{bcp}}$. ^e Estimated by the eq 6 of ref 23, using as a and b parameters the ab initio values computed in a periodic calculation on the crystal of DMACB. ^f At $-X$, $1 - Y$, $+Z$. ^g At $1 - X$, $1 - Y$, $+Z$. ^h At $-1 + X$, $+Y$, $+Z$. ⁱ At $-1/2 + X$, $1/2 - Y$, $1 - Z$. ^j At $-1/2 + X$, $1/2 - Y$, $-Z$. ^k At $1 + X$, $+Y$, $+Z$. ^l At $1/2 + X$, $1/2 - Y$, $-Z$.

**Figure 4.** $V(\mathbf{r})_{\text{bcp}}$ vs $G(\mathbf{r})_{\text{bcp}}$ for the intermolecular hydrogen bonds of (1). Values are in units of kJ mol^{-1} per atomic unit volume. The straight-line equation resulting from the least-squares fit is also reported.

There is a very good linear correlation between the $G(\mathbf{r})_{\text{bcp}}$ and $V(\mathbf{r})_{\text{bcp}}$ values (Figure 4), in agreement with the ab initio results found by Espinosa et al. for a series of molecular dimers with weak HBs.²⁵ The same authors showed also that, for closed-shell interactions, the hydrogen bond energy E_{HB} (defined as $-D_e$, where D_e is the hydrogen bond dissociation energy) may be correlated to the $V(\mathbf{r})_{\text{bcp}}$ value by a simple change of scale. They derived a simple empirical relationship from theoretical results on molecular dimers, which in atomic units is:

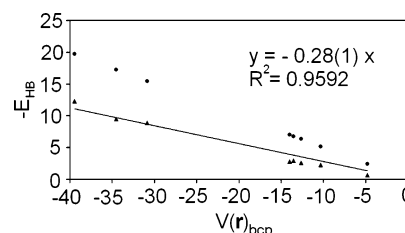
$$E_{\text{HB}} = 0.5 \cdot V(\mathbf{r})_{\text{bcp}} \quad (3)$$

More recently a crystal of 3,4-bis(dimethylamino)-3-cyclobutene-1,2-dione (DMACB), containing 23 unique $\text{CH}\cdots\text{O}$ interactions and no other kind of competing $\text{XH}\cdots\text{O}$ HBs, has been studied.²³ It has been found that the $\text{CH}\cdots\text{O}$ bond energies of DMACB largely deviate from the values obtained by eq 3, and a new equation was successfully applied to this case:

$$E_{\text{HB}} = V(\mathbf{r})_{\text{bcp}} \cdot \left(\frac{a_c}{a} \right) \cdot \exp[(b - b_e) \cdot d_{\text{H}\cdots\text{O}}] \quad (4)$$

where a , a_e , b , and b_e are parameters resulting from previous least-squares fits relating $V(\mathbf{r})_{\text{bcp}}$ and E_{HB} with $d_{\text{H}\cdots\text{O}}$.

The last two columns of Table 3 report the $-E_{\text{HB}}$ values for the eight intermolecular HBs of (1) derived from the experimental topological indicators through eqs 3 and 4, respectively. It can be seen that both the models agree in predicting the two $\text{OH}\cdots\text{O}$ HBs and the $\text{C9-H3}\cdots\text{O2}$ HB as the most attractive bonds. The plotting of the two estimates of E_{HB} versus $V(\mathbf{r})$ for

**Figure 5.** Values of the experimental hydrogen bond energy (in kJ mol^{-1}) as estimated by the eqs 3 (circles) and 4 (triangles) vs the local potential energy density at the bcp (in kJ mol^{-1} per atomic unit volume). Both $\text{CH}\cdots\text{O}$ and $\text{OH}\cdots\text{O}$ intermolecular HBs are considered. The straight line equation resulting from the least-squares fit of the values from eq 4 is reported, with the constraint that $E_{\text{HB}} = 0$ when $V(\mathbf{r})_{\text{bcp}} = 0$.

all the HBs (Figure 5) emphasizes that (i) $\text{OH}\cdots\text{O}$ and $\text{CH}\cdots\text{O}$ HBs follow precisely the same linear trend, further adding to the evidence that they behave very much alike; (ii) the difference between E_{HB} values from the two methods becomes higher and higher as the absolute value of $V(\mathbf{r})_{\text{bcp}}$ increases, i.e., while increasing the strength of the interaction.

The values of $\text{CH}\cdots\text{O}$ interaction energies reported in the literature²² range between 0.85 and 1.2 kJ mol^{-1} , for the case of very weak HBs, and 9.5 kJ mol^{-1} , for polarized bonds: it can be seen that, in the case of (1), the proposed estimates are in the correct range, the only deviation being the exceptionally strong $\text{C9-H3}\cdots\text{O2}$ bond. This confirms the great similarity between the $\text{C9-H3}\cdots\text{O2}$ and the $\text{OH}\cdots\text{O}$ HBs pointed out in the previous sections on geometrical and topological grounds, and proves that molecules of (1) are strongly packed in the (a , b) plane (dimers C, D, and E), whereas in the c direction, they are connected by weaker forces (dimers A and B). The two $\text{OH}\cdots\text{O}$ and the $\text{C9-H3}\cdots\text{O2}$ intermolecular HBs are crucial in determining the occurrence of the C_2 axis along c , which leads to the uncommon space group $P2_12_12_1$. In the Cambridge Structural Database (CSD⁶⁵), indeed, until January 2005, there were only 1482 entries for this space group (corresponding to 0.45% of the total structures deposited), whereas for the more common $P2_12_12_1$, the entries were 27630 (8.33%). In the present case, the unusual crystal symmetry is dictated by the favorable formation of hydrogen-bonded ribbons in the (a , b) plane. By contrast, citrinin,⁵⁹ another fungal metabolite whose core structure is similar to that of austdiol, shows no clear pattern of strong HBs in a crystallographic plane, and packs in the $P2_12_12_1$ space group.

We note also that, on going from RT to 70 K, the unit cell parameters reduce anisotropically, with a reduction of 0.4% for a and b and of 2.2% for c . The larger unit cell contraction along the c axis suggests that the strengthening of the $\text{CH}\cdots\text{O}$ interactions along this direction is the driving force that leads to the cell volume reduction upon cooling.

3.3. Electrostatic Properties. **3.3.1. Molecular Dipole Moments.** The electric multipole moments are compact summaries of the *total* molecular charge distribution (i.e., they account for both the positive and negative charges) and can provide insight into the nuclear and electronic structure of molecules.⁶⁶

The magnitude of the molecular dipole moment μ (Table 4) does not change upon crystallization, the experimental module being equal to the MG-B3LYP values within 1 s.u. for both the single-point and the optimized geometry. Nevertheless, upon packing, a noticeable charge rearrangement is observed. Indeed, while in the isolated molecule, μ lies almost entirely in the main molecular plane, in the crystal, the angle between μ and the normal to the least-squares plane defined by all the endocyclic

TABLE 4: Molecular Dipole Moment of (1) Evaluated from the Experimental Electron Density at 70 K and from Theoretical Calculations on the Isolated Molecule (Optimized and Experimental Geometry)^a

	μ_x	μ_y	μ_z	$ \mu $
experimental	-1(2)	3(1)	-3.8(5)	4.8(9)
MG-B3LYP opt ^b	3.6028	3.8407	0.2262	5.2709
MG-B3LYP exp ^c	3.6430	4.3315	0.2673	5.6661

^a All values are given in Debye, with experimental s.u. in parentheses. The component values are expressed in Cartesian coordinates and are referred to the eigenvectors of the inertial tensor, with the origin in the molecular center of mass. ^b DFT B3-LYP 6-31G(pd) calculation on the isolated molecule (optimized geometry). ^c DFT B3-LYP 6-31G(pd) calculation on the isolated molecule (experimental geometry).

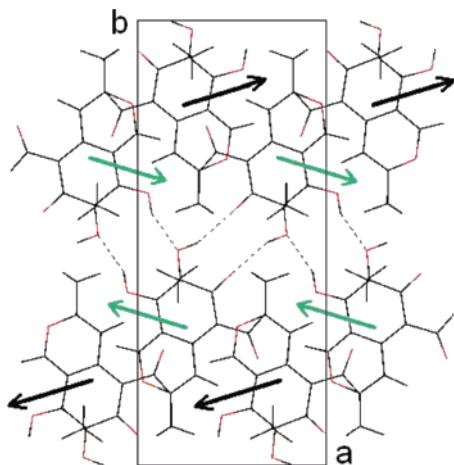


Figure 6. Crystal packing view along *c* of (1), the experimental dipole moment direction of the austdiol molecules being indicated. Dashed lines represent the OH \cdots O hydrogen bonding in the (*a*, *b*) plane. Light arrows designate dipole vectors pointing outside the paper, while dark arrows indicate vectors directed inside the picture.

atoms is 41(12)°. The angle between the experimental and the MG-B3LYP dipole vector amounts to about 71°.

In the crystallographic (*a*, *b*) plane, where molecules are related by *C*₂ axes, adjacent rows of dipoles along *b* maximize their electrostatic attractive energy, arranging themselves in an antiparallel fashion (Figure 6, light arrows). This is indeed the direction of the most favorable intermolecular HBs. Along the *a* axis, molecules are related by 2-fold screw axes and head-to-tail chains of dipoles pointing alternately up and down are formed.

3.3.2. Electrostatic Potential. The features of the experimental molecular electrostatic potential $\varphi(\mathbf{r})$ of (1) are depicted in Figure 7. Five regions of negative potential are visible in the (*a*, *b*) plane around each of the five oxygen atoms, ranging from -0.01 e \AA^{-1} down to -0.1 e \AA^{-1} : as known, sign and magnitude of $\varphi(\mathbf{r})$ provide information on the relative imbalance between the influence of nuclei and electrons in the vicinity of a molecule (i.e., electropositive and electronegative regions). The deepest and more extended minimum in the mapped plane amounts to $-0.11(7)$ e \AA^{-1} and is found at 1.277 Å from the O2 aldehyde oxygen, corroborating the results of the previous sections, i.e., the high affinity of this atom for hydrogen bond formation. On the other hand, the particular morphology of $\varphi(\mathbf{r})$ in the region between H1 and O2 is a characteristic signature of intramolecular hydrogen bonding and confirms that this is the only intramolecular HB in the crystal.

3.3.3. Energies of Intermolecular Interactions. The calculation of accurate intermolecular interaction energies (E_{int}) is of great importance in evaluation of a host of physical properties,

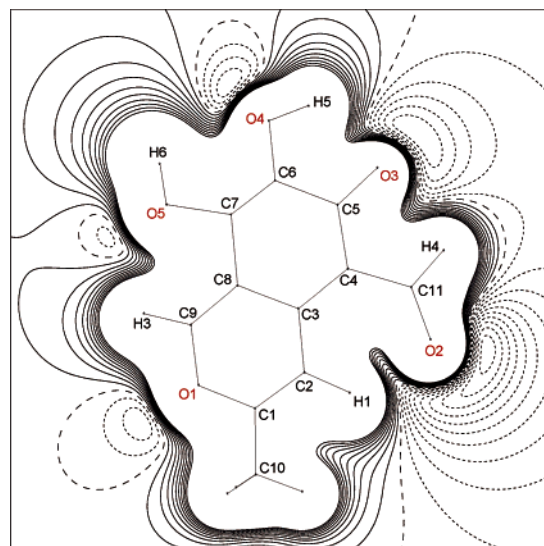


Figure 7. Experimental electrostatic potential of (1) extracted from the crystal. The contour map (12 Å × 12 Å) is shown in the (*a*, *b*) plane. Contours are plotted at intervals of 0.01 e \AA^{-1} (1 e \AA^{-1} \equiv 332.1 kcal mol⁻¹). Negative and zero contours: short and long dashed lines, respectively; positive contours: solid lines. All the atoms within 0.55 Å from the plane are labeled.

including lattice energies of molecular crystals, and has important implications for crystal structure prediction strategies. Interaction energies are computed as the difference in energy between the dimer, on one hand, and the sum of isolated monomers, on the other hand:

$$E_{\text{int}} = E(\text{AB}) - (E(\text{A}) + E(\text{B})) \quad (5)$$

There are a variety of ways in which E_{int} can be partitioned, but the scheme that has received the most use over the years in theoretical calculations is the Morokuma–Ziegler decomposition scheme:^{67,68}

$$E_{\text{int}} = E_{\text{es}} + E_{\text{Pauli}} + E_{\text{oi}} \quad (6)$$

where E_{es} is the electrostatic interaction energy defined by the exact potential (EP), E_{Pauli} is the exchange repulsion, and E_{oi} (orbital interaction energy) includes charge transfer and polarization effects. Conversely, when the starting point is an X-ray charge density distribution, the most convenient and accurate formalism is that devised by Spackman,^{69,70–72} where E_{int} is partitioned as follows:

$$E_{\text{int}} = E_{\text{es}} + E_{\text{rep}} + E_{\text{disp}} + E_{\text{pen}} \quad (7)$$

Here, E_{es} is calculated according to the Buckingham-type (moment–moment, MM) approach,⁷³ the repulsion (E_{rep}) and dispersion (E_{disp}) terms are approximated by using *exp*-6 atom–atom potentials, and E_{pen} , the penetration electrostatic contribution, is defined as the interaction of the spherical charge distribution of one molecule with the deformation charge density of the second. Regardless of the choice of the partitioning scheme, it is known that the electrostatic interaction energy E_{es} is one of the most significant contributions to the total binding energy, especially in the case of crystals containing polar molecules.

Theoretical and experimental estimates of this contribution for the five hydrogen-bonded dimers of (1) (Figure 8) are summarized in Table 5 in order of increasing distance between the centers of mass of the two molecules. The first column reports experimental values of E_{es} , as obtained from the

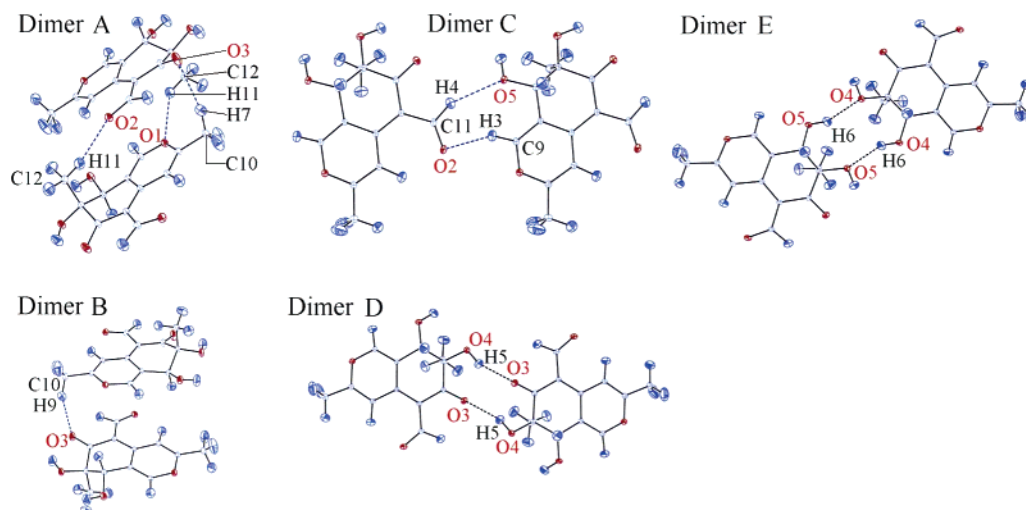


Figure 8. ORTEP plot of five hydrogen-bonded dimers of (1). Ellipsoids at 50% probability. Intermolecular HBs are represented as dashed lines.

TABLE 5: Comparison between the Electrostatic Contribution (E_{es} , kJ mol^{-1}) to the Total Interaction Energies for the Five Hydrogen-Bonded Dimers of (1) as Evaluated with Different Methods

dimer	d_{CM} (Å) ^a	E_{es} (exp) ^b	E_{es} (P-B3LYP) ^c	E_{es} (MA-BLYP) ^d
A	5.712	−19(4)	−26	−28
B	5.809	−29(3)	−25	−27
C	8.417	−13(3)	−18	−27
D	8.632	−26(4)	−26	−28
E	8.689	−32(5)	−38	−53

^a Distance between centers of mass of the molecules in a dimer.

^b Electrostatic energy obtained through eq 8 (see text) applied to the experimental $\rho(\mathbf{r})$. s.u. of the $E_{\text{def-def}}$ term in parentheses. ^c As above, but starting from the theoretical $\rho(\mathbf{r})$ obtained from P-B3LYP structure factors. ^d Electrostatic contribution to the interaction energy, obtained from MA-BLYP calculations on the isolated dimers (program ADF^{49,50}).

multipolar X-ray $\rho(\mathbf{r})$ through the MM approximation corrected for the promolecule energy, following the strategy recently proposed by Spackman.⁷⁴ In this new approach, E_{es} is expressed as a sum of promolecule–promolecule, promolecule–deformation, and deformation–deformation terms:

$$E_{\text{es}} = E_{\text{pro-pro}} + E_{\text{def-def}} + E_{\text{pro-def}} \quad (8)$$

where $E_{\text{pro-pro}}$ involves a sum over Coulombic interactions between pairs of spherical atomic charge densities and can be determined as a function of the separation, $E_{\text{def-def}}$ is the old MM electrostatic component of eq 7, arising from the deformation terms of the molecular charge distribution, and $E_{\text{pro-def}}$ is the old E_{pen} component of eq 7. The $E_{\text{def-def}}$ term has been evaluated via the atom-centered multipole expansion up to the hexadecapole–hexadecapole term in the Cartesian tensor formulation. The second column of Table 5 lists the values of E_{es} obtained in the same way, but starting from the calculated charge density distribution in the crystal obtained from P-B3LYP structure factors. All these energies have been calculated with the PAMOC program.⁷⁵ The third column reports the electrostatic interaction energies as obtained with the program ADF^{49,50} for the isolated dimers.

It is worthwhile to note that, in all the dimers, the $E_{\text{pro-pro}}$ term is significantly larger and more negative than the quantity $E_{\text{es}}(\text{MM})$, as evaluated according to the Buckingham-type approach. In particular, for dimers from B to E, $E_{\text{pro-pro}}$ contributes from 72 to 85% to the total (attractive) electrostatic

TABLE 6: Comparison between the Total Intermolecular Interaction Energies (E_{int} , kJ mol^{-1}) for the Five Hydrogen-Bonded Dimers of (1) as Evaluated with Different Methods

dimer	d_{CM} (Å) ^a	E_{int} (exp) ^b	E_{int} (P-B3LYP) ^c	E_{int} (MA-BLYP) ^d	E_{int} (MG-B3LYP) ^e
A	5.712	5(4)	−2	19	12
B	5.809	−6(3)	−3	14	9
C	8.417	4(3)	−2	−6	−9
D	8.632	−10(4)	−10	3	−3
E	8.689	−8(5)	−14	−28	−35

^a Distance between centers of mass of the molecules in a dimer.

^b Interaction energy obtained through eq 7 (see text) applied to the experimental $\rho(\mathbf{r})$. s.u. of the E_{es} term in parentheses. ^c As above, but starting from the theoretical $\rho(\mathbf{r})$ obtained from P-B3LYP structure factors. ^d Interaction energy, corrected for BSSE with the counterpoise method, obtained from MA-BLYP calculations on the isolated dimers with the Morokuma–Ziegler decomposition scheme implemented in the ADF program. ^e Interaction energy, corrected for BSSE with the counterpoise method, obtained from MG-B3LYP calculations on the isolated dimers as $E_{\text{int}} = E(\text{AB}) - (E(\text{A}) + E(\text{B}))$.

energy, while in dimer A, where the $E_{\text{es}}(\text{MM})$ term is repulsive (+5 kJ mol^{-1}), the $E_{\text{pro-pro}}$ contribution (−24 kJ mol^{-1}) makes attractive the total electrostatic energy.

From inspection of Table 5, it can be seen that: (i) for all the five dimers, E_{es} are always negative; (ii) the agreement between the experimental and theoretical estimates of E_{es} by eq 8 is excellent, the differences never exceeding 1.75 s.u.; (iii) the new Spackman model for E_{es} predicts the correct relative electrostatic interaction energies (third column) in the majority of cases, the only exception being dimer C, which is significantly less attractive in both the crystal calculations than in the isolated dimer. As expected, the highest value in modulus is found for dimer E, where the two identical OH...O HBs related by a C_2 axis account for the energetically most favorable dimer configuration.

Table 6 shows E_{int} values evaluated as follows: through eq 7 applied to the experimental (first column) and theoretical (second column) $\rho(\mathbf{r})$ in the crystal; through eq 6 applied to ADF MA-BLYP calculations (third column), and through eq 5 applied to supermolecule MG-B3LYP calculations (fourth column). The values in the last two columns take into account the correction for the BSSE through the counterpoise method.⁵⁴ It can be seen that: (i) the agreement between the experimental and theoretical estimates of E_{int} by eq 7 is still very good, the maximum difference being twice the experimental s.u.. (ii)

Differences between E_{int} values from eqs 5 and 6 on isolated dimers are small, both the approaches predicting repulsive interactions for pairs bonded along the c direction (dimers A and B) and attractive interactions in the (a, b) plane (dimers C, D, and E). This is an expected result, in view of what was found in Section 3.2.3 in terms of hydrogen bond energetics. (iii) Conversely, the discrepancies between the estimates obtained on the crystal (first and second column) and those obtained on isolated dimers (third and fourth column) are large and significant, and have to be imputed to matrix effects.

4. Conclusions

We have shown that the topological analysis of the experimental and theoretical charge density of (**1**), together with the study of the intermolecular interaction energies, are very effective instruments to address similarities and differences between OH \cdots O and CH \cdots O interactions. Furthermore, with such tools, we could rank the strength of OH \cdots O and CH \cdots O HBs present in this crystal on a relative scale and give experimental evidence that CH \cdots O HBs behave very much like the conventional OH \cdots O HBs in most respects.

In particular: (1) We have found that the two simple packing rules proposed in ref 18 are well satisfied for (**1**). All the exocyclic O atoms in the molecule are involved as hydrogen bond acceptors in true HBs, which engage most of the H atoms. The interplay between intra- and intermolecular HBs and between OH \cdots O and CH \cdots O interactions has been elucidated, and it has been shown that HB acceptors compete for being saturated by the most favorable HBs. This is particularly evident by comparing the theoretical topology of the gas-phase molecule with that in the crystal: the intramolecular OH \cdots O AIL found in the isolated molecule disappears in the crystal, where the O atoms compete for more favorable OH \cdots O intermolecular HBs.

(2) The observed crystal packing, which leads to the uncommon space group $P2_12_12_1$, is governed by the strength of the intermolecular interactions and not by the chemical nature of the HB donors involved. Indeed, the tight ribbon pattern in the (a, b) plane is set up by the cooperative arrangement of two OH \cdots O and one CH \cdots O HBs of comparable strength, while the looser packing in the perpendicular direction is dictated by the formation of weaker, less favorable interactions. This fact explains well the anisotropic reduction of cell volume upon cooling: the major contraction along the c axis is caused by the strengthening of the weak CH \cdots O interactions along this direction, whereas the strongest HBs in the (a, b) plane are not affected by the temperature.

(3) Despite the overall weakness of CH \cdots O HBs with respect to OH \cdots O, they fit essentially the same features, including the dependence of both the XHO angular distribution and $\rho_{\text{bcp}}(\mathbf{r})$ from the $d_{\text{H}\cdots\text{O}}$ distance. The case of the exceptionally strong C9–H3 \cdots O2 HB shows that the similarity between CH \cdots O and OH \cdots O HBs may be also quantitative.

The comparison between experimental and theoretical electric multipole moments reveals that a noticeable charge rearrangement occurs upon crystallization, and shows the effects of the mutual cooperation of HBs in the crystal. Finally, the new model proposed by Spackman for the evaluation of the electrostatic contribution to the intermolecular interaction energy has been successfully applied to an experimental charge density distribution, and appears to be a very powerful tool for the study of hydrogen-bonded crystals.

Acknowledgment. We thank Prof. F. Aragozzini of the University of Milan, Italy, for the provision of crystals. We

gratefully acknowledge also Dr. L. Belvisi and Dr. D. Invernizzi of the Organic and Industrial Chemistry Department (University of Milan, Italy) for assistance in the molecular mechanics calculations and Dr. M. Barzaghi of CNR-ISTM (Milan) for help with ADF calculations and fruitful discussions.

Supporting Information Available: A complete description of the data treatment, together with full lists of experimental bond distances, bond angles, and torsion angles at 70 K. Full details of the theoretical calculations (MM and ab initio) and lists of the optimized geometries. A brief discussion on the atomic charges. A full list of the topological indicators at the bond critical points (bcp's) of all the covalent bonds and at the ring critical points (rcp's); maps of the experimental $\rho(\mathbf{r})$ and its negative Laplacian $\nabla^2\rho(\mathbf{r})$ in the (a, b) plane. This material is available free of charge via the Internet at <http://pubs.acs.org>.

References and Notes

- (1) Jeffrey, G. A. *An Introduction to Hydrogen Bonding*; Oxford University Press: New York, 1997.
- (2) Desiraju, G. R. *Angew. Chem., Int. Ed. Engl.* **1995**, *34*, 2311–2327.
- (3) Aakeröy, C. B. *Acta Crystallogr., Sect. B* **1997**, *53*, 569–586.
- (4) Desiraju, G. R. *Chem. Commun.* **1997**, *16*, 1475–1482.
- (5) Dunitz, J. D. *Chem. Commun.* **2003**, *5*, 545–548.
- (6) Motherwell, W. D. S.; Ammon, H. L.; Dunitz, J. D.; Dzyabchenko, A.; Erk, P.; Gavezzotti, A.; Hofmann, D. W. M.; Leusen, F. J. J.; Lommerse, J. P. M.; Mooij, W. T. M.; Price, S. L.; Scheraga, H.; Schweizer, B.; Schmidt, M. U.; van Eijck, B. P.; Verwer, P.; Williams, D. E. *Acta Crystallogr., Sect. B* **2002**, *58*, 647–661.
- (7) Dunitz, J. D.; Filippini, G.; Gavezzotti, A.; *Helv. Chim. Acta* **2000**, *83*, 2317–2335.
- (8) Dunitz, J. D. *Chem.—Eur. J.* **1998**, *4*, 745–746.
- (9) Ferretti, V.; Bertolasi, V.; Pretto, L. *New J. Chem.* **2004**, *28*, 646–651.
- (10) Kojic-Prodic, B.; Peric, B.; Stefanic, Z.; Meden, A.; Makarevic, J.; Jokic, M.; Zinic, M.; *Acta Crystallogr., Sect. B* **2004**, *60*, 90–96.
- (11) Csöregi, I.; Weber, E.; Finge, S. *Cryst. Eng.* **2002**, *5*, 59–70.
- (12) Baudron, S. A.; Batail, P.; Rovira, C.; Canadell, E.; Clérac, R. *Chem. Commun.* **2003**, *15*, 1820–1821.
- (13) Jetty, R. K. R.; Thallapally, P. K.; Xue, F.; Mak, T. C. W.; Nangia, A. *Tetrahedron* **2000**, *56*, 6707–6719.
- (14) Dapporto, P.; Paoli, P.; Roelens, S. J. *Org. Chem.* **2001**, *66*, 4930–4933.
- (15) Etter, M. C. *J. Phys. Chem.* **1991**, *95*, 4601–4610.
- (16) Taylor, R.; Macrae, C. F. *Acta Crystallogr., Sect. B* **2001**, *57*, 815–827.
- (17) Pratt Brock, C. *Acta Crystallogr., Sect. B* **2002**, *58*, 1025–1031.
- (18) Bertolasi, V.; Gilli, P.; Ferretti, V.; Gilli, G. *Acta Crystallogr., Sect. B* **2001**, *57*, 591–598.
- (19) Steiner, T. *Chem. Commun.* **1997**, *8*, 727–734.
- (20) Steiner, T.; Desiraju, G. R. *Chem. Commun.* **1998**, *8*, 891–892.
- (21) Koch, U.; Popelier, P. L. A. *J. Phys. Chem.* **1995**, *99*, 9747–9754.
- (22) Gu, Y.; Kar, T.; Scheiner, S. J. *Am. Chem. Soc.* **1999**, *121*, 9411–9422.
- (23) Gatti, C.; May, E.; Destro, R.; Cargnoni, F. *J. Phys. Chem. A* **2002**, *106*, 2707–2720.
- (24) Munshi, P.; Guru Row, T. N. *J. Phys. Chem. A* **2005**, *109*, 659–672.
- (25) Espinosa, E.; Molins, E.; Lecomte, C. *Chem. Phys. Lett.* **1998**, *285*, 170–173.
- (26) Bader, R. F. W. *Atoms in Molecules: A Quantum Theory*; Oxford University Press: Oxford, 1990.
- (27) Gatti, C. Z. *Kristallogr.* **2005**, *220*, 399–457.
- (28) Abramov, Y. A. *Acta Crystallogr., Sect. A* **1997**, *53*, 264–272.
- (29) Abramov, Y. A.; Volkov, A.; Wu, G.; Coppens, P. *J. Phys. Chem. B* **2000**, *104*, 2183–2188.
- (30) Steyn, P. S. *Tetrahedron* **1973**, *29*, 107–120.
- (31) Vleggaar, R.; Steyn, P. S.; Nagel, D. W. *J. Chem. Soc., Perkin Trans. 1* **1974**, 45–49.
- (32) Steyn, P. S.; Vleggaar, R. *J. Chem. Soc., Perkin Trans. 1* **1976**, 204–206.
- (33) Nielsen, K. F.; Smedsgaard, J. J. *Chromatogr., A* **2003**, *1002*, 111–136.
- (34) Frisvald, J. C.; Thrane, U. *J. Chromatogr.* **1987**, *404*, 195–214.
- (35) Colombo, L.; Gennari, C.; Poli, G.; Scolastico, C.; Aragozzini, F.; Merendi, C. *J. Chem. Soc., Perkin Trans. 1* **1983**, 2745–2749 and references therein.

- (36) Lo Presti, L.; Soave, R.; Destro, R. *Acta Crystallogr., Sect. C* **2003**, 59, 199–201.
- (37) Engel, D. W.; Kruger, G. J. *Acta Crystallogr., Sect. B* **1976**, 32, 2545–2548.
- (38) Destro, R. *Aust. J. Phys.* **1988**, 41, 503–510.
- (39) Samson, S.; Goldish, E.; Dick, C. J. *J. Appl. Crystallogr.* **1980**, 13, 425–432.
- (40) The data collection temperature deserves a special note: X-ray diffraction data for **(1)** were initially collected at 23 K, but their analysis showed several anomalies. Subsequent investigations proved that, at $T < 70$ K, the crystal of **(1)** undergoes an unexpected and complex series of phase transitions. A discussion of the nature of these transitions goes beyond the purposes of this paper and will be the topic of a further, detailed study. For this reason, a new X-ray data collection has been performed at $T = 70$ K. The present paper relates to this set of data.
- (41) Stewart, R. F. *Acta Crystallogr., Sect. A* **1976**, 32, 565–574.
- (42) Stewart, R. F.; Spackman, M. A.; Flensburg, C. *VALRAY User's Manual*, version 2.1; Carnegie Mellon University: Pittsburgh; University of Copenhagen: Copenhagen, 2000.
- (43) Roversi, P.; Destro, R. *Chem. Phys. Lett.* **2004**, 386, 472–478.
- (44) Hirshfeld, F. L. *Acta Crystallogr., Sect. A* **1976**, 32, 239–244.
- (45) The rigid-body analysis was performed with a local program based on the treatment of (a) Schomaker, V.; Trueblood, K. N. *Acta Crystallogr., Sect. B* **1968**, 24, 63–76, and (b) Dunitz, J. D.; Schomaker, V.; Trueblood, K. N. *J. Phys. Chem.* **1988**, 92, 856–867. The performance of our code has been repeatedly verified by comparison with that of the code THMA, (c) Schomaker, V.; Trueblood, K. N. *Acta Crystallogr., Sect. B* **1998**, 54, 507–514.
- (46) Mohamadi, F.; Richards, N. G. J.; Guida, W. C.; Liskamp, R.; Lipton, M.; Caufield, C.; Chang, G.; Hendrickson, T.; Still, W. C. *J. Comput. Chem.* **1990**, 11, 440–467.
- (47) Allinger, N. L. *J. Am. Chem. Soc.* **1977**, 99, 8127–8134.
- (48) Frisch, M. J.; Trucks, G. W.; Schlegel, H. B.; Scuseria, G. E.; Robb, M. A.; Cheeseman, J. R.; Zakrzewski, V. G.; Montgomery, J. A., Jr.; Stratmann, R. E.; Burant, J. C.; Dapprich, S.; Millam, J. M.; Daniels, A. D.; Kudin, K. N.; Strain, M. C.; Farkas, O.; Tomasi, J.; Barone, V.; Cossi, M.; Cammi, R.; Mennucci, B.; Pomelli, C.; Adamo, C.; Clifford, S.; Ochterski, J.; Petersson, G. A.; Ayala, P. Y.; Cui, Q.; Morokuma, K.; Malick, D. K.; Rabuck, A. D.; Raghavachari, K.; Foresman, J. B.; Cioslowski, J.; Ortiz, J. V.; Stefanov, B. B.; Liu, G.; Liashenko, A.; Piskorz, P.; Komaromi, I.; Gomperts, R.; Martin, R. L.; Fox, D. J.; Keith, T.; Al-Laham, M. A.; Peng, C. Y.; Nanayakkara, A.; Gonzalez, C.; Challacombe, M.; Gill, P. M. W.; Johnson, B. G.; Chen, W.; Wong, M. W.; Andres, J. L.; Head-Gordon, M.; Replogle, E. S.; Pople, J. A. *Gaussian 98*, revision A.11.3; Gaussian, Inc.: Pittsburgh, PA, 2002.
- (49) Te Velde, G.; Bickelhaupt, F. M.; Baerends, E. J.; Fonseca Guerra, C.; Van Gisbergen, S. J. A.; Snijders, J. G.; Ziegler, T. *J. Comput. Chem.* **2001**, 22, 931–967.
- (50) *ADF2004.01*; SCM, Theoretical Chemistry, Vrije Universiteit: Amsterdam, The Netherlands, 2004; (<http://www.scm.com>).
- (51) Becke, A. D. *J. Chem. Phys.* **1993**, 98, 5648–5652.
- (52) Lee, C.; Yang, W.; Parr, R. G. *Phys. Rev. B* **1988**, 37, 785–789.
- (53) Becke, A. D. *Phys. Rev. A* **1988**, 38, 3098–3100.
- (54) Boys, S. F.; Bernardi, F. *Mol. Phys.* **1970**, 19, 553–566.
- (55) Saunders, V. R.; Dovesi, R.; Roetti, C.; Orlando, R.; Zicovich-Wilson, C. M.; Harrison, N. M.; Doll, K.; Civalieri, B.; Bush, I. J.; D'Arco, Ph.; Llunell, M. *CRYSTAL2003 User's Manual*; University of Torino: Torino, Italy, 2003.
- (56) Burnett, M. N.; Johnson, C. K. *ORTEP III, Oak Ridge Thermal Ellipsoid Plot Program for Crystal Structure Illustrations*; Report ORNL-6895; Oak Ridge National Laboratory: Oak Ridge, Tennessee, 1996.
- (57) Cremer, D.; Pople, J. A. *J. Am. Chem. Soc.* **1975**, 97, 1354–1358.
- (58) Bader, R. F. W.; Slee, T. S.; Cremer, D.; Kraka, E. *J. Am. Chem. Soc.* **1983**, 105, 5061–5068.
- (59) Roversi, P.; Barzaghi, M.; Merati, F.; Destro, R. *Can. J. Chem.* **1996**, 74, 1145–1161.
- (60) By the topological analysis of $\rho(\mathbf{r})$, it has been found that the angles between the eigenvector associated with the λ_2 curvature of the short C1–C10 bond and those of the adjacent C1–C2 and C1–O1 bonds are 23° and 38°, respectively, both significantly lower than the values calculated for the other exocyclic C6–C12 methyl bond with the adjacent C6–C7 (48°), C5–C6 (82°), and O4–C6 (81°) bonds. This suggests that some hyperconjugative interaction occurs between the C10 methyl and the unsaturated system of **(1)**, inducing a slight double bond character in what is formally a single bond and justifying the lower value of the bond distance.
- (61) (a) Mascal, M. *Chem. Commun.* **1998**, 3, 303–304; (b) Bondi, A. *J. Phys. Chem.* **1964**, 68, 441–451.
- (62) Jeffrey, G. A.; Saenger, W. *Hydrogen Bonding in Biological Structures*; Springer: Berlin, 1991.
- (63) (a) Koritsanszky, T. S.; Coppens, P. *Chem. Rev.* **2001**, 101, 1583–1627; (b) Coppens, P. *X-ray Charge Densities and Chemical Bonding*; Oxford University Press: New York, 1997.
- (64) Bilton, C.; Allen, F. H.; Shields, G. P.; Howard, J. A. K. *Acta Crystallogr., Sect. B* **2000**, 56, 849–856.
- (65) Allen, F. H. *Acta Crystallogr., Sect. B* **2002**, 58, 380–388.
- (66) Spackman, M. A. *Chem. Rev.* **1992**, 92, 1769–1797.
- (67) Ziegler, T.; Rauk, A. *Theor. Chim. Acta* **1977**, 46, 1–10.
- (68) Morokuma, K. *J. Chem. Phys.* **1971**, 55, 1236–1244.
- (69) Spackman, M. A.; Weber, H. P.; Craven, B. M. *J. Am. Chem. Soc.* **1988**, 110, 775–782.
- (70) Spackman, M. A. *J. Chem. Phys.* **1986**, 85, 6579–6586.
- (71) Spackman, M. A. *J. Chem. Phys.* **1986**, 85, 6587–6601.
- (72) Spackman, M. A. *J. Phys. Chem.* **1987**, 91, 3179–3186.
- (73) (a) Buckingham, A. D. In *Physical Chemistry: An Advanced Treatise*; Henderson, D., Ed.; Academic Press: New York, 1970; pp 349–386; (b) Buckingham, A. D. In *Intermolecular Interactions: From Diatomics to Biopolymers*; Eds.: B. Pullmann, B., Ed.; Wiley and Sons: Chichester, New York, 1978, pp 1–67.
- (74) Spackman, M. A. *Chem. Phys. Lett.* **2005**, 418, 154–158.
- (75) Barzaghi, M. *PAMoC, Online User's Manual*, version 2002.0; CNR-ISTM, Institute of Molecular Science and Technologies: Milano, Italy, 2002; URL: www.istm.cnr.it/~barz/pamoc/